

Sea Surface Salinity Signature of the Tropical Atlantic Interannual Climatic Modes

F. M. Awo, G. Alory, C. Y. Da-Allada, T. Delcroix, J. Jouanno, E. Kestenare, E. Baloïtcha

▶ **To cite this version:**

F. M. Awo, G. Alory, C. Y. Da-Allada, T. Delcroix, J. Jouanno, et al.. Sea Surface Salinity Signature of the Tropical Atlantic Interannual Climatic Modes. Journal of Geophysical Research. Oceans, 2018, 123, pp.7420-7437. 10.1029/2018JC013837 . insu-03683065

HAL Id: insu-03683065

https://insu.hal.science/insu-03683065

Submitted on 1 Jun 2022

HAL is a multi-disciplinary open access archive for the deposit and dissemination of scientific research documents, whether they are published or not. The documents may come from teaching and research institutions in France or abroad, or from public or private research centers.

L'archive ouverte pluridisciplinaire **HAL**, est destinée au dépôt et à la diffusion de documents scientifiques de niveau recherche, publiés ou non, émanant des établissements d'enseignement et de recherche français ou étrangers, des laboratoires publics ou privés.

Copyright

Journal of Geophysical Research: Oceans

RESEARCH ARTICLE
10.1029/2018JC013837

Sea Surface Salinity Signature of the Tropical Atlantic Interannual Climatic Modes

F. M. Awo[1,2,3], G. Alory[2], C. Y. Da-Allada[1,3,4,5], T. Delcroix[2], J. Jouanno[2], E. Kestenare[2], and E. Baloïtcha[1]

[1]CIPMA, Université d'Abomey Calavi, Cotonou, Bénin, [2]LEGOS, UMR CNES, CNRS, IRD, Université de Toulouse, Toulouse, France, [3]LHMC/IRHOB/IRD, Cotonou, Bénin, [4]IRD/LOPS, IFREMER, CNRS, Université de Brest, IUEM, Brest, France, [5]ESTBR/UNSTIM, Abomey, Bénin

Key Points:
- The SSS signature of the tropical Atlantic meridional and equatorial interannual modes is extracted from in situ observations
- Oceanic/atmospheric processes driving the signature of each mode are identified through a mixed-layer salt budget in a validated model
- The SSS signatures of the meridional and equatorial modes are well captured by SMOS satellite during particular events

Correspondence to:
F. M. Awo,
mesmin.awo@gmail.com

Citation:
Awo, F. M., Alory, G., Da-Allada, C. Y., Delcroix, T., Jouanno, J., Kestenare, E., & Baloïtcha, E. (2018). Sea surface salinity signature of the tropical Atlantic interannual climatic modes. *Journal of Geophysical Research: Oceans*, *123*, 7420–7437. https://doi.org/10.1029/2018JC013837

Received 25 JAN 2018
Accepted 10 SEP 2018
Accepted article online 17 SEP 2018
Published online 21 OCT 2018

Abstract The characteristic sea surface salinity (SSS) patterns associated with the tropical Atlantic meridional and equatorial interannual modes are extracted from in situ observations, by a statistical analysis performed on the 1980–2012 period. These SSS signatures of the interannual climatic modes are reproduced in a regional numerical simulation. For each mode, oceanic and/or atmospheric processes driving the SSS signature are identified through a mixed-layer salt budget in the validated model. During a positive meridional mode in spring, a northward shift of the Intertropical Convergence Zone and related precipitation maximum creates a south-north dipole of positive-negative SSS anomalies around the equator. Western boundary currents strengthen and advect relatively fresh equatorial waters, which creates negative SSS anomalies in the north and south west tropical Atlantic. Meridional and vertical advection create positive SSS anomalies off the Congo River. During a positive equatorial mode in summer, a southward shift of the Intertropical Convergence Zone-related rainfall maximum creates a south-north dipole of negative-positive SSS anomalies between the equator and 10°N. Meridional advection also contributes to the positive SSS anomalies between 5°N and 10°N. Vertical advection and diffusion at the mixed-layer base create positive SSS anomalies between 5°S and the equator. Horizontal advection creates large SSS anomalies in the North Brazil Current retroflection region, negative along the coast and positive further offshore. The SSS signatures of the meridional and equatorial modes described above are well captured by the Soil Moisture–Ocean Salinity satellite during the 2010 and 2012 events.

Plain Language Summary This study shows that both meridional and equatorial interannual climatic modes impact the sea surface salinity (SSS) in tropical Atlantic through atmospheric and/or oceanic processes. The atmospheric forcing, related to Intertropical Convergence Zone migration, controls the equatorial region, while the advection, due to modulation of current dynamics, vertical SSS gradient, and mixing at the base of mixed layer, drives SSS in the region under the influence of river plumes.

1. Introduction

Sea surface salinity (SSS) is an essential climate variable that can affect oceanic circulation through seawater density (Gasparin & Roemmich, 2016; Gelderloos et al., 2012; Maes, 1998). In the tropics, low SSS regions are often associated with strong surface stratification that can strengthen ocean-atmosphere interactions (Bosc et al., 2009; Grodsky et al., 2012; Maes et al., 2005). SSS also bears the signature of the marine hydrological cycle (e.g. Schanze et al., 2010; Schmitt, 1995, 2008; Terray et al., 2012; Yu, 2011). In particular, its long-term trends reflect the intensification of the hydrological cycle in a warming climate (Curry et al., 2003; Durack et al., 2012; Durack & Wijffels, 2010; Hosoda et al., 2009; Levang & Schmitt, 2015).

In tropical Atlantic, the mean SSS has a very contrasted distribution (Figure 1) with low SSS around 5°N due to strong precipitation under the Intertropical Convergence Zone (ITCZ), high SSS near the center of large-scale subtropical gyres where evaporation (E) dominates over precipitation (P; Gordon et al., 2015). In addition, strong freshwater discharges by the Amazon, Congo, and Niger rivers create low SSS plumes (Figure 1). The SSS seasonal cycle is maximum around these plumes, with an opposite phase in the Amazon region and in the Congo-Niger region, partly controlled by freshwater inputs in the Amazon region only (Tzortzi et al., 2013). Da-Allada et al. (2013), Da-Allada, du Penhoat, et al. (2014), and Camara et al. (2015) have recently revisited the SSS seasonal cycle through observations and salt budget in models. They found that SSS is

©2018. American Geophysical Union. All Rights Reserved.

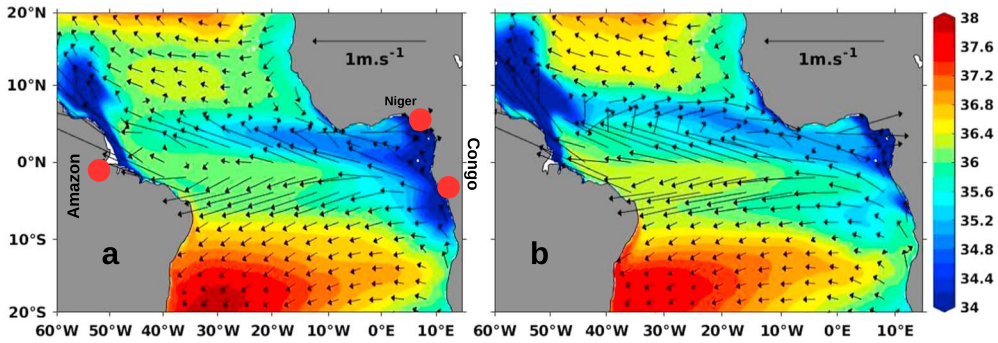


Figure 1. Boreal (a) spring and (b) summer SSS (shadings) and surface current (arrows) from model. The positions of the three major rivers (the Amazon, the Congo, and the Niger) are indicated as red circles in Figure 1a. SSS = sea surface salinity.

driven by both oceanic and atmospheric processes and the balance differs from one region to another. In boreal spring and summer, in the northeast tropical Atlantic, zonal advection, associated with the North Equatorial Counter Current (NECC), and precipitation, linked to ITCZ seasonal variation, mainly control the balance. However, in the northwest tropical Atlantic and Gulf of Guinea (GG), where there are strong horizontal gradients and strong currents (North Brazil Current, Guinea Currents, and South Equatorial Current; see Figure 1), it is mainly controlled by horizontal advection, vertical diffusion, and entrainment. In the Congo region, it is mainly driven by vertical processes due to strong vertical gradients.

While the seasonal cycle of tropical Atlantic SSS is now rather well documented, little is known of its interannual variability due to a lack of relatively long observational records in tropical Atlantic, compared to the North Atlantic (e.g., Friedman et al., 2017; Mignot & Frankignoul, 2004; Reverdin et al., 2007). Using observations collected from research vessels and Voluntary Observing Ships (VOS), Dessier and Donguy (1994) dealt with this problem. They found that SSS variability is mainly controlled by precipitation due to the ITCZ in the eastern Atlantic, while it is mainly due to freshwater outflow from the Amazon and Orinoco rivers in the west. Da-Allada, du Penhoat, et al. (2014) extended these results in the GG with an oceanic model. They showed that in the GG north of the equator, changes in SSS are first driven by changes in precipitation associated with the ITCZ migration and second by wind-forced changes in currents that affect horizontal and vertical advection, as well as vertical diffusion due to current shear. However, south of the equator, farther from the ITCZ influence and with no interannual variations in the Congo runoff considered in the model, wind forcing was found to be the main driver.

Results based on analysis of sea surface temperature (SST) and surface winds interannual anomalies have shown that interannual climate variability in the tropical Atlantic Ocean is dominated by a meridional mode and an equatorial mode (Foltz & McPhaden, 2010; Xie & Carton, 2004). The meridional mode peaks in boreal spring as an interhemispheric SST fluctuation (Kushnir et al., 2006). The equatorial mode, often viewed as the Atlantic counterpart to the Pacific El Niño Southern Oscillation (ENSO), peaks in boreal summer and creates SST anomalies in the GG (Kushnir et al., 2006).

Both modes involve some ocean-atmosphere coupling. The meridional mode appears to be mainly driven by thermodynamics through wind-induced evaporation and positive wind-evaporation-SST feedback (Chang et al., 1997). In contrast, SST anomalies associated with the equatorial mode are mainly driven by ocean dynamics, as reflected in the strong positive correlation between sea level and SST anomalies in the eastern equatorial Atlantic (Hu & Huang, 2006; Keenlyside & Latif, 2007). Like ENSO, the equatorial mode is nevertheless driven by the positive Bjerknes feedback between SST, zonal wind, and thermocline depth (Keenlyside & Latif, 2007).

Both modes are associated with surface wind anomalies. During a positive meridional mode, the tropical Atlantic warming in the north and cooling in the south drives southerly surface wind anomalies, resulting in a northward migration of the ITCZ (Murtugudde et al., 2001; Nobre & Shukla, 1996). During a positive equatorial mode, westerly wind anomalies precede the positive SST anomalies in the GG (Lübbecke et al., 2010; Richter et al., 2013). These anomalies correspond to a relaxation of trade winds in the west equatorial region, which leads to a southward migration of ITCZ. These ITCZ migrations affect rainfall regimes in the tropical

Atlantic with strong impacts on the surrounding countries. The positive phase of the meridional mode results in higher precipitation in the West African Sahel and northern South America and, on the contrary, less precipitation in the GG and the Amazon basin. During its positive phase, the equatorial mode is associated with higher rainfall in the northern GG (Kushnir et al., 2006).

Beside their impact on precipitation, interannual modes also influence ocean circulation. The ITCZ migration related to the meridional mode affects the Guinea Dome in fall (Doi et al., 2009). Moreover, Hormann et al. (2012) observed a relationship between NECC variability and these modes. They found that the NECC shifts northward during the positive phase of the meridional mode, while it strengthens during the negative phase of the equatorial mode. It means that these modes can potentially influence the processes driven by oceanic currents, such as heat and salt advection and diffusion that occur in the mixed layer.

As these modes affect precipitation and currents, they can also affect SSS large-scale variability, in the same way that Pacific SSS is related to ENSO (e.g., Delcroix & Hénin, 1991; Hasson et al., 2013; Singh et al., 2011). To our knowledge, the impact of these modes on tropical Atlantic SSS has not been studied yet. Reverdin et al. (2007) and Friedman et al. (2017) highlighted the impact of climatic modes like ENSO, North Atlantic Oscillation, and Atlantic Multidecadal Oscillation on Atlantic SSS but did not establish any link between SSS and the meridional and equatorial Atlantic modes. Their study essentially focused on the North Atlantic where collected in situ data were long enough to analyze interannual or decadal changes. However, Tchilibou et al. (2015) showed that the mean position of the E-P minimum, associated with the ITCZ, closely matches an SSS minimum in tropical Atlantic and that, at interannual time scale, the E-P and SSS minima have a similar meridional migration, mainly driven by the meridional mode.

The goal of the present study is to identify the SSS signature (the signature is here defined as the typical pattern and amplitude of SSS anomalies) of the two tropical Atlantic interannual modes with in situ observations and investigate the main driving mechanisms (oceanic and/or atmospheric) responsible for it using an ocean general circulation model. The observations, numerical simulation, and methodologies used in this study are described in section 2. Section 3 provides results, including SSS signature, model validation, and process studies. Special attention is given to the regions where oceanic contribution is important, in particular, the impact of changes in surface current. Section 4 provides a summary and a discussion of the most important results.

2. Data and Methods

For the analysis, in situ data, satellite data, reanalysis products, and a regional numerical simulation are used.

2.1. Data

2.1.1. In Situ Data

An updated version of the Atlantic (30°S–50°N; 1970–2013) SSS product described in Reverdin et al. (2007) is used. This 1° × 1° × 1-month gridded product is based on an objective analysis of in situ SSS data. This product is mainly based on observations from thermosalinographs installed on board VOS (Alory et al., 2015) research vessels and sailing ships, Prediction and Research Moored Array in the Atlantic (PIRATA) moorings and Argo floats (since 2004), surface drifters, and few cruise-derived Conductivity- Temperature-Depth (CTD) casts. This results in a heterogeneous coverage with high density along three Europe-South America and Europe-South Africa VOS lines and low density south of 10°S, which produces data gaps in the gridded product (see http://dx.doi.org/10.6096/SSS-LEGOS-GRID-ATL). Regions with temporal data coverage lower than 50% are reported in our figures. Also, due to the low density of observations during the 1970s, data from 1980 only are used in this study.

2.1.2. Satellite Data

We use data from the Soil Moisture–Ocean Salinity (SMOS) satellite mission (Boutin et al., 2016). In this study we use the so-called L3_DEBIAS_LOCEAN_v1 SSS fields produced at Laboratoire d'Océanographie et du Climat : Expérimentations et Approches Numériques (LOCEAN) and distributed by Centre Aval de Traitement des Donnees SMOS. This product is available on a 0.25 × 0.25° grid at weekly time scale from July 2010 to March 2016, and the systematic coastal biases have been removed (Kolodziejczyk et al., 2016). The spatial and temporal decorrelation scales deduced from SMOS are consistent with other satellite products in tropical Atlantic (Tzortzi et al., 2016). As the calibration of the instrument was not stable and the polarization mode was not fixed in the first months of the SMOS mission (Boutin et al., 2016), we also removed in July–August 2010 a bias of 0.15 that appeared in the comparison with in situ data.

2.1.3. Reanalysis Products

The monthly SST, wind, evaporation, and precipitation reanalysis products are derived from the European Center for Medium Range Weather Forecasts (ECMWF) ERA-Interim reanalysis (Dee et al., 2011). We used the full 1979–2016 period available.

2.1.4. Model

The model used here is the Nucleus for European Modeling of the Ocean (NEMO3.6) ocean general circulation model described by Madec and the NEMO team (2016). It solves three-dimensional primitive equations in spherical coordinates discretized on a C-grid and at fixed vertical levels. The regional configuration used here covers tropical Atlantic with a horizontal resolution of 1/4° and provides daily outputs. The model is forced at the lateral boundaries with daily outputs of the second global ocean Mercator reanalysis version 3 (GLORYS2V3) (Ferry et al., 2012). On the vertical, the model resolves 75 levels, with 24 levels in the upper 100 m. The salinity budget terms in the mixed layer are computed online and averaged daily. The model has been integrated from 1958 to 2015, but only outputs for the 1980–2012 period are used in this study, so that they can be compared with observations. This configuration has already been used for salinity studies by Da-Allada et al. (2017) within the GG and Hernandez et al. (2016) in the Amazon-Orinoco river plume region. The atmospheric fluxes are provided by bulk formulae (Large & Yeager, 2004) and DRAKKAR Forcing Set 5.2 (DFS5.2) product (Dussin et al., 2016). There is neither SSS restoring nor SST restoring in this simulation. The monthly climatology of continental runoff from Dai and Trenberth (2002) is prescribed for surface freshwater flux near each river mouth. The use of climatological runoff is justified by Berger et al. (2014), who tested different simulations with interannual river flows and found that their interannual variability do not have much effect on interannual SSS variability within the eastern tropical Atlantic Ocean, which seems also to be true off the Amazon River (Mama & Alory, 2011). For further details regarding parameterization and some elements of validation, including comparisons with in situ observations, one can refer to Hernandez et al. (2017) for temperature and mixed-layer depth and Da-Allada, du Penhoat, et al. (2014) and Da-Allada et al. (2017) for salinity variations.

2.2. Methodology

2.2.1. Empirical Orthogonal Function and Regression Analysis

As the meridional and equatorial modes are respectively the dominant interannual signals in boreal spring and summer (Foltz & McPhaden, 2010), driven by ocean-atmosphere interactions where SST and wind play a key role (Chang et al., 1997; Keenlyside & Latif, 2007), we performed a multivariate empirical orthogonal function (EOF) analysis (e.g., Alory & Delcroix, 2002) on boreal spring and summer SST and wind anomalies (relative to the monthly mean climatology) to extract their covarying patterns. An individual EOF analysis of SST and wind variations did not show significantly different results, and the multivariate analysis allows to present results in a more synthetic way. We finally computed annual time series of SSS averaged over the peak season of each mode, that is, spring (March–April–May) for the meridional mode and summer (June–July–August) for the equatorial mode. To extract the SSS signature of each interannual mode, we then regressed these seasonally averaged SSS time series onto the normalized temporal function of the first EOF mode of the SST-wind multivariate analysis, as SSS can be indirectly affected by both SST (through convection and related precipitation) and wind (through evaporation or currents) variations related to these modes. The regression method on SSS made it easier to deal with in situ data gaps; however, a regression or EOF analysis of the model SSS gives similar results, as will be shown later. A test of the 90% level significance of the correlation associated with the regression analysis, taking into account the number of observations, was systematically performed and reported in our figures.

2.2.2. SSS Budget

To investigate processes driving SSS anomalies in our regional simulation, we used the mixed-layer salinity budget terms computed online in the model. Mixed-layer budget has been widely used in ocean surface processes studies, for instance, in SST within the tropical Atlantic Ocean (e.g., Jouanno et al., 2011) and for SSS within the western tropical Atlantic Ocean (Ferry & Reverdin, 2004) and the GG (Berger et al., 2014; Da-Allada, Alory, et al., 2014; Da-Allada, du Penhoat, et al., 2014; Da-Allada et al., 2017; Camara et al., 2015).

For the SSS budget, we relied on the following mixed-layer salinity evolution equation:

$$\partial_t SSS = -\underbrace{\langle u\partial_x S\rangle}_{\text{ADU}} - \underbrace{\langle v\partial_y S\rangle}_{\text{ADV}} - \underbrace{\langle w\partial_z S\rangle}_{\text{ADW}} + \underbrace{D_l(S)}_{\text{DIFL}} - \underbrace{\frac{(k_z\partial_z S)_{z=-1}}{h}}_{\text{DIFV}} - \underbrace{\frac{1}{h}\frac{\partial h}{\partial t}(SSS - S_{z=-h})}_{\text{ENT}} + \underbrace{\frac{(E-P-R)SSS}{h}}_{\text{FWF}} \quad (1)$$

with $\langle . \rangle = \frac{1}{h}\int . dz$.

where S is the model salinity and u, v, and w are the components of the current in the zonal (positive eastward), meridional (positive northward), and vertical (positive upward) direction, respectively. $D_l(S)$ is the lateral diffusion operator, k_z is the vertical diffusion coefficient, h is the mixed-layer depth, E is evaporation, P is precipitation, and R is river runoff. The terms in equation (1) represent, from left to right, mixed-layer salinity tendency, zonal advection (ADU), meridional advection (ADV), vertical advection (ADW), horizontal diffusion (DIFL), vertical diffusion at the mixed-layer base (DIFV), mixed-layer salinity tendency due to entrainment at the mixed-layer base (ENT), and freshwater flux forcing (FWF). All terms are computed explicitly in the model except for the entrainment term that is estimated as a residual.

2.2.3. Integration Method

To link the spring SSS signature of the meridional mode and the summer SSS signature of the equatorial mode, extracted through the methodology described above, and the SSS budget, several steps were necessary. First, we integrated the SSS budget terms of the mixed-layer salinity equation (1) from winter (December–January–February [DJF]) to spring (March–April–May [MAM]) and from spring to summer (June–July–August [JJA]) through equations (2) and (3), respectively. Second, we regress the results onto the temporal function of each mode to extract the associated processes. The details of the integration method are given in Appendix A.

$$\underbrace{\frac{1}{92}\sum_{i=93}^{184} S_{-33+i}}_{\bar{S}_{\mathrm{MAM}}} = \underbrace{\frac{1}{92}\sum_{i=1}^{92} S_{-33+i}}_{\bar{S}_{\mathrm{DJF}}} + \frac{1}{92}\left[\sum_{i=1}^{92} i\times\Delta S_{-33+i} + \sum_{i=1}^{92}(92-i)\times\Delta S_{59+i}\right] \tag{2}$$

$$\underbrace{\frac{1}{92}\sum_{i=93}^{184} S_{59+i}}_{\bar{S}_{\mathrm{JJA}}} = \underbrace{\frac{1}{92}\sum_{i=1}^{92} S_{59+i}}_{\bar{S}_{\mathrm{MAM}}} + \frac{1}{92}\left[\sum_{i=1}^{92} i\times\Delta S_{59+i} + \sum_{i=1}^{91}(92-i)\times\Delta S_{151+i}\right] \tag{3}$$

Here S_i is the daily mean of mixed-layer salinity for calendar day i, and $\Delta S_i = \frac{\mathrm{d}S}{\mathrm{d}t_i}\Delta t$ with $\mathrm{d}S/\mathrm{d}t_i$ the tendency. $\bar{S}_{\mathrm{DJF}}$, $\bar{S}_{\mathrm{MAM}}$, and $\bar{S}_{\mathrm{JJA}}$ are the winter, spring, and summer mean SSS anomalies, respectively. Number 92 denotes the number of days in one season; see Appendix A for other numbers. The last two terms represent the integrated SSS budget terms of equation (1) from winter to spring and from spring to summer, respectively. This relation links the observed SSS signature and the model evolution equation (1) that we will use later to quantify the contribution of each process.

3. Results

3.1. SST and Wind Interannual Modes of Variability

To set the context, the SST and wind spatiotemporal structures of the meridional and equatorial modes during their peak season, as extracted from observations by a multivariate EOF analysis, are shown in Figure 2. In spring, the first EOF mode accounts for 29.3% of the interannual variance, whereas in summer, it accounts for 20.5% of the interannual variance.

The dominant spring mode (Figure 2a or 2b) shows an interhemispheric SST gradient with positive anomalies north of a slightly southwest-northeast tilted line near the equator and negative anomalies to the south. The associated wind pattern shows basin-wide northward wind anomalies, corresponding to a strengthening of the southeast trade winds and a relaxation of the northeast trade winds. These characteristics define the meridional mode (Servain et al., 1999; and Foltz & McPhaden, 2010). Values outside 1 standard deviation range in the normalized time function (Figure 2c) indicate the occurrence of a well-marked meridional mode, either positive in 1981, 1983, 1992, 1997, 2004, 2005, and 2012 or negative in 1984, 1985, 1986, 1989, 1996, 2008, and 2009.

The dominant summer mode is characterized by an anomalous SST warming particularly strong in the GG, with westerly wind anomalies corresponding to a relaxation of trade winds in the west equatorial region (Figure 2d or 2e). These characteristics define the equatorial mode (Foltz & McPhaden, 2010). Values outside the standard deviation range in the normalized time function (Figure 2f) indicate the occurrence of an equatorial mode, either positive in 1988, 1989, 1995, 1996, 1999, 2008, and 2010 or negative in 1982, 1983, 1992, 1994, 1997, 2002, 2014, and 2015. A similar EOF analysis performed on the simulation outputs gives patterns very consistent with observations (Figure 2). Similarly, the first EOF mode accounts for 31.2% of the

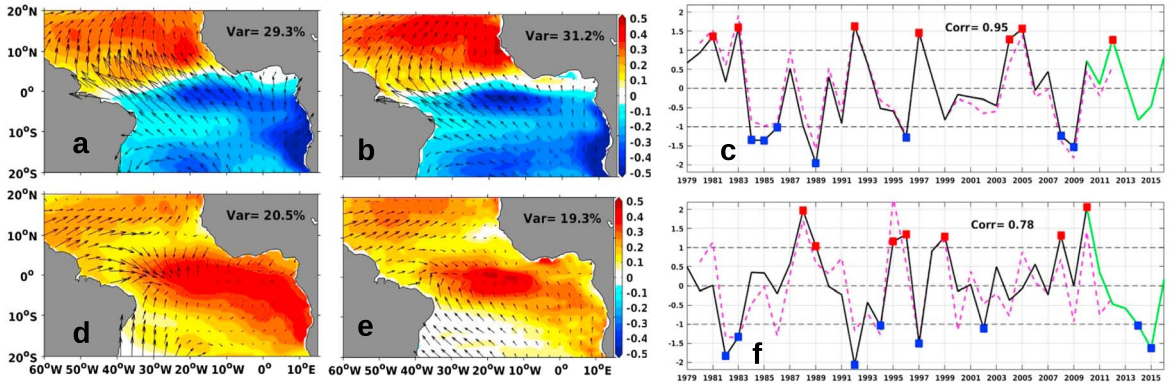


Figure 2. First combined EOF analysis maps performed on SST-wind anomalies in boreal (a, b) spring and (d, e) summer from ERA-Interim reanalysis (a, d; black lines in the time series), model (b, e; dashed magenta lines in the time series), and (c, f) their respective normalized time series for the 1979–2016 period. The green lines in the time series correspond to the SMOS period. Red and blue dots in the time series denote values in excess of ±1 standard deviation. EOF = empirical orthogonal function; SST = sea surface temperature; ERA = European Center for Medium Range Weather Forecasts (ECMWF) Reanalysis; SMOS = Soil Moisture–Ocean Salinity.

interannual variability in spring and 19.3% in summer. The correlations between the model and observation time functions reach 0.95 for the meridional mode and 0.78 for the equatorial mode, both significant at the 95% level. The wind anomalies, likely to affect currents and evaporation, combined with ITCZ-related rainfall anomalies also associated with these modes (Carton & Huang, 1994; Hastenrath & Greischar, 1993; Nobre & Shukla, 1996; Servain et al., 1999) and large river discharges in tropical Atlantic, suggest that these modes can also affect SSS. This expected impact is explored in the next section.

3.2. SSS Signature of the Meridional and Equatorial Modes

Using the regression method defined in section 2.2.1, we extracted the SSS signature related to the meridional and equatorial modes from the in situ product (Figures 3a and 3d) and the model simulation (Figures 3b and 3e). Generally, the model reproduces relatively well the results from the in situ product especially in regions with strong SSS anomalies represented by boxes in Figure 3. However, the model shows smoother patterns, probably due to its homogeneous grid strongly contrasting with the much more heterogeneous coverage of observations. We also performed an EOF analysis on the model SSS anomalies (Figures 3c and

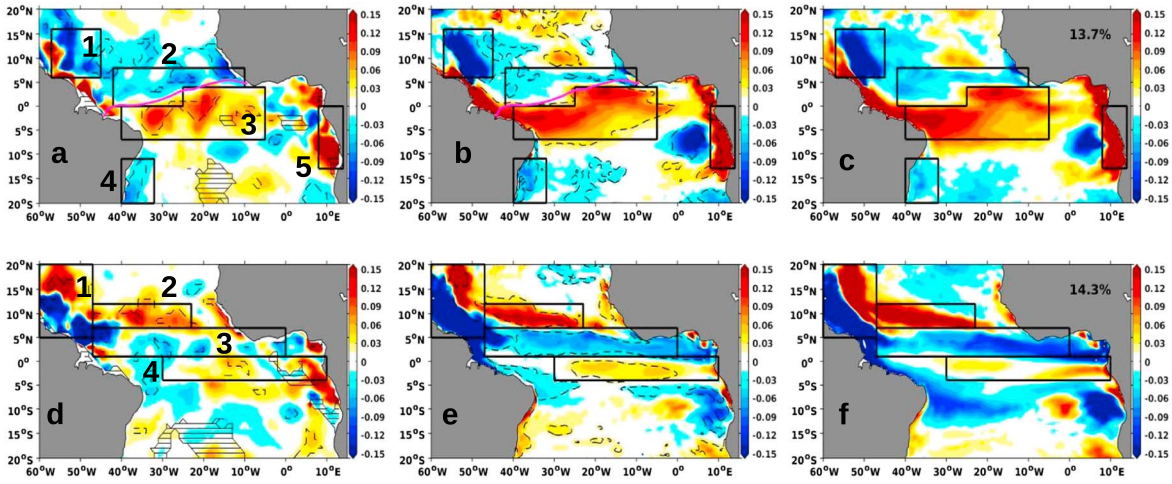


Figure 3. SSS signature of the positive phase of the (a–c) meridional and (d–f) equatorial modes from (a, d) in situ observations and (b, c, e, f) model. Figures 3a, 3b, 3d, and 3e represent regression coefficients of SSS anomalies onto the meridional and equatorial modes' time function, respectively (Figures 2c and 2f, black lines), and Figures 3c and 3f represent the dominant pattern mode of the EOF analysis performed on SSS anomalies in spring and summer, respectively. The front between positive/negative SST anomalies in Figure 2a is superposed on Figures 3a and 3b (magenta line). Regions 1 to 5 delimited by heavy black lines are discussed in the main text. The (a, d) hatched zones denote regions where the available data density is less than 50%. The dashed black contours represent the 90% significance threshold. SSS = sea surface salinity; EOF = empirical orthogonal function; SST = sea surface temperature.

3f). The patterns of the dominant modes correspond well to the regression maps in Figure 3, and their time functions are strongly correlated to the meridional and equatorial modes time functions of Figures 2c and 2f (correlation values are 0.84 and 0.60, respectively, both significant at the 95% level). This suggests that the SSS signatures are due to a physical coupling with SST and wind rather than imposed by the statistical analysis. As expected, the results of a multivariate EOF analysis combining SSS, SST, and wind give results even closer to the regression analysis (not shown).

Comparing model and observations, we, however, notice slight differences (around 0.03 pss) in the south tropical region between 5–20°S and 30°W–10°E for both the meridional (Figures 3a and 3b) and equatorial (Figures 3d and 3e) modes. These differences may be due, on the one hand, to the inability of the model to reproduce well the observations and, on the other hand, to the low density of in situ observations in this region (Figure 1 in Reverdin et al., 2007; Figure 1 in Da-Allada et al., 2013). We will therefore mainly focus on the boxes represented in Figure 3, where observed SSS anomalies are strong and significant and reproduced by the model in both the regression and EOF analyses.

During the positive phase of the meridional mode (Figures 3a–3c), a north-south dipole of SSS anomalies appears along the equatorial region, with positive and negative anomalies around 5°S (box 3) and 5°N (box 2), respectively. The equatorial frontal zone in SSS (Figures 3a and 3b, magenta lines) remarkably matches the SST front (Figure 2a). Negative SSS anomalies also appear off the South American coast around 15°S (box 4) and 10°N (box 1) where they are particularly strong. Positive SSS anomalies appear off the African coast with a maximum around 10°S (box 5). SSS anomalies of opposite sign appear during the negative phase of the meridional mode.

The equatorial mode (Figures 3d–3f) has an SSS signature different from the meridional mode. During its positive phase, there are zonal bands of SSS anomalies that are positive around 10°N (box 2), negative around 5°N (box 3), and then positive again around the equator (box 4). Strong negative SSS anomalies appear at 10°N off the South American coast (box 1), with positive SSS anomalies found further offshore seemingly connected with those in box 2. SSS anomalies of opposite sign appear during the negative phase of the equatorial mode.

3.3. The 2010 and 2012 SSS Anomalies From In Situ and SMOS Products

To confirm that the SSS signature of interannual modes extracted from EOF analyses are real rather than statistical artifacts, SSS anomalies in summer 2010 and spring 2012, which are peak periods of positive equatorial and meridional modes, respectively (see Figures 2c and 2f), are shown in Figure 4. Moreover, since these two events are included in both the SMOS and in situ products availability period, we compare the SSS anomalies observed in each product.

For the meridional mode, a good correspondence is observed between the previously extracted SSS signature (Figure 3a) and spring 2012 in situ anomalies (Figure 4a), especially in the boxes. In addition, there is a good agreement between the in situ and SMOS products, although the latter appears noisier due to its finer resolution. In the areas where in situ data are not available, especially off the Congo and Amazon rivers, SMOS fills the gap with anomalies very consistent with the SSS signature of the meridional mode, notably in box 5 (compare Figures 3a and 4b).

The expected SSS signature of the equatorial mode (Figure 3c) is also observed in summer 2010 in both the in situ and SMOS products (Figures 4c and 4d), in particular, the positive anomaly in boxes 2 and 4 and the negative anomaly in box 1. In boxes 2 and 3, SMOS SSS anomalies are more consistent with the expected signature than in situ anomalies, probably due to the better spatial coverage of the satellite product.

The agreement between in situ and SMOS data is, however, weaker for the equatorial than the meridional mode, which may be due to the fact that SSS anomalies are weaker in 2010 than in 2012 and also that 2010 was the first year of the SMOS mission, with instrument calibration still problematic (Boutin et al., 2016). Overall, despite its relatively short time period, SMOS captures remarkably well the patterns of interannual variability and is very complementary to in situ observations.

3.4. Processes Responsible for the SSS Signature

To identify processes responsible for the SSS signature of interannual modes previously shown, we integrate from one season to the next the model mixed-layer salinity budget, following equations (1)–(3) above. Like

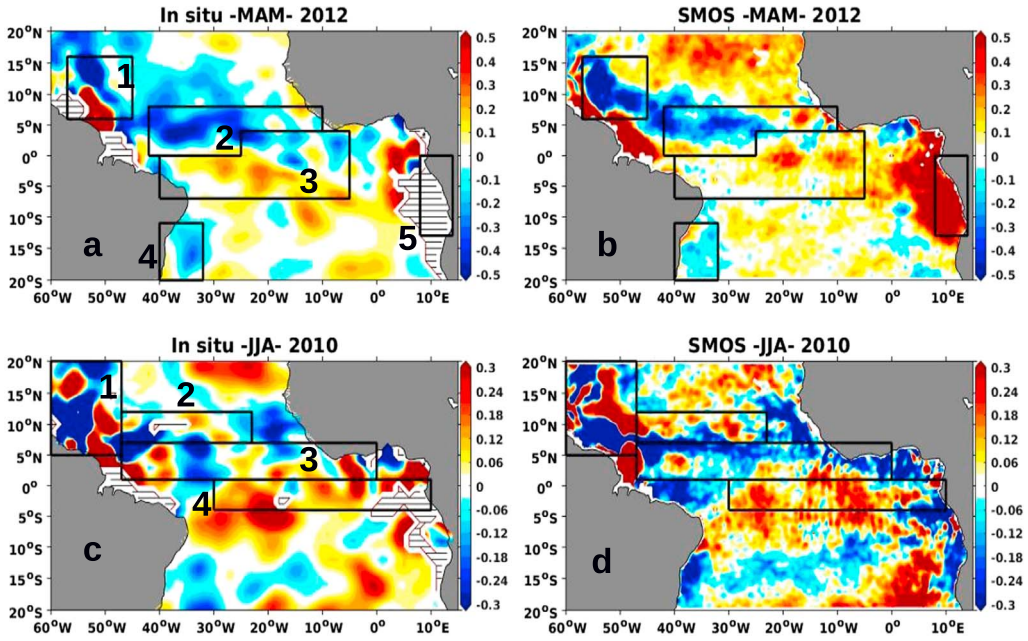


Figure 4. SSS anomalies in (a, b) spring 2012 and (b, d) summer 2010 from in situ (a, c) and SMOS satellite observations (c, d). The (a, c) hatched zones denote regions where there are no in situ observations. Regions 1 to 5 are as in Figure 3. SSS = sea surface salinity; SMOS = Soil Moisture–Ocean Salinity; MAM = March–April–May; JJA = June–July–August.

SST and wind anomalies, model SSS anomalies related to the meridional and equatorial modes peak in spring (MAM) and summer (JJA), respectively (Figure 5). They can be directly attributed to the integrated budget terms through equations (2) and (3), as Figure 5 shows that anomalies are pretty small in the previous season, which allows us to neglect them.

3.4.1. Meridional Mode

The winter-to-spring integrated tendency term (Figure 6a) compares well with the SSS signature in the model (Figure 3b), especially in the boxes, which validates our methodology. The slight differences in amplitude observed mainly in the equatorial boxes is due to winter anomalies that are not totally negligible. The SSS tendency (Figure 6a) results from the contribution of different processes: atmospheric forcing (Figure 6b), horizontal advection (Figure 6c) that includes the zonal and meridional components, and subsurface processes (Figure 6d) that combines vertical advection and diffusion. The lateral diffusion and entrainment terms are not represented as their contribution is negligible.

The salt budget shows that the negative and positive SSS anomalies observed in equatorial boxes 2 and 3, respectively, during a positive meridional mode, are mainly due to atmospheric forcing (Figure 6b). Our analysis shows that in box 2, E-P decreases, whereas it increases in box 3. This gradient of E-P anomalies is found around the mean latitude of the ITCZ in spring and due to its northward shift associated with a positive meridional mode (Murtugudde et al., 2001). As the ITCZ corresponds to a maximum in rainfall, this shift brings more rain into box 2 where SSS then decreases and less rain in box 3 where SSS increases. The ITCZ also corresponds to a meridional minimum in wind, so as it shifts northward wind and related evaporation weaken in box 2 and strengthen in box 3, which also contribute to the meridional SSS anomalies gradient. In the ERA-Interim product, precipitation anomalies are, however, 10 times as large as evaporation anomalies (not shown). The simultaneous meridional migration of the ITCZ-related E-P and SSS minima during the meridional mode was previously documented (Tchilibou et al., 2015). Moreover, horizontal advection related to the South Equatorial Current has a contribution in box 2, which partly reduces the SSS decrease due to the atmospheric forcing.

In boxes 1 and 4 off the South American coast, negative SSS anomalies are mainly due to horizontal advection (Figure 6c). Indeed, in these two boxes, there are strong negative anomalies in the horizontal advection term, whereas anomalies are weaker and of opposite sign in the subsurface process term and far weaker in the

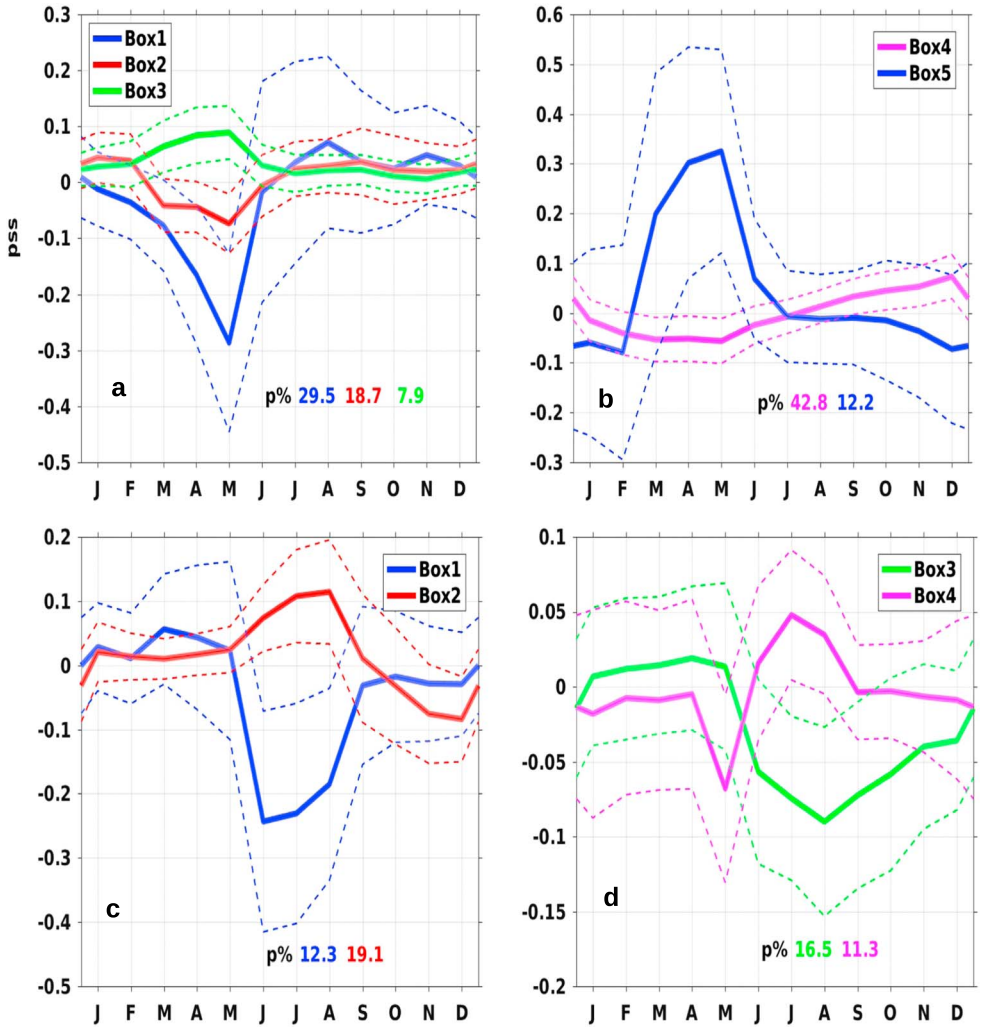


Figure 5. Time series of model SSS anomalies in boxes 1 to 5 (see Figure. 3) related to the (a, b) meridional and (c, d) equatorial modes, obtained by regressing the box-averaged interannual SSS anomalies for each calendar month onto the spring meridional mode or summer equatorial mode time series shown in Figures 2c and 2f. In Figure 5c, only negative anomalies are averaged in box 1. The dashed lines represent the uncertainty range at 90% significance threshold. The explained variance (p in percentage) of SSS anomalies in meridional mode season (spring; a, b) or equatorial mode season (summer; c, d) by their preseason SSS anomalies winter and spring, respectively). SSS = sea surface salinity.

surface forcing term. To better understand the advection processes, the zonal and meridional advection were further analyzed by splitting the impact of the mean seasonal currents and SSS field and their interannual anomalies. The zonal advection anomalies can be decomposed as follows:

$$-u \cdot s_x - \underbrace{(-\overline{u} \cdot \overline{s}_x)}_{\text{I}} = \underbrace{-u' \cdot \overline{s}_x}_{\text{II}} \underbrace{-\overline{u} \cdot s'_x}_{\text{III}} \underbrace{-u's'_x}_{\text{IV}} \tag{4}$$

where $\overline{X} = (\overline{u}, \overline{s})$ denotes the seasonal-mean component (computed on the 1980–2012 period) and $X' = (u', s')$ the relative interannual variation (Hasson et al., 2014; Zhang et al., 2016). Term II represents the advection anomaly generated by the zonal current anomalies, term III the advection anomaly generated by the SSS gradient anomalies, and term IV the advection anomaly generated by the combined SSS gradient and currents anomalies. Meridional advection can be also decomposed in the same way.

The temporal evolution of SSS and horizontal advection anomalies (Figure 7) confirms that the negative SSS anomalies that develop from winter and peak during the spring meridional mode are mainly due to

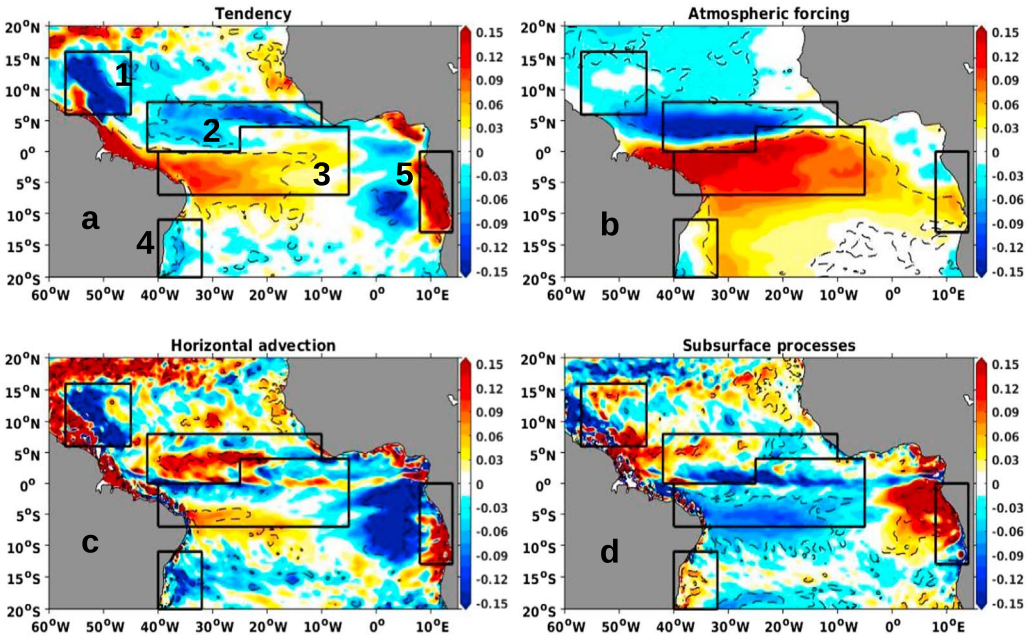


Figure 6. Winter to spring mixed-layer salinity budget (pss) for the meridional mode: (a) tendency term, (b) atmospheric forcing, (c) horizontal advection, and (d) subsurface processes. Figures 6a–6d represent regression coefficients of salinity budget term anomalies onto the meridional mode time function shown in Figure 2c. The dashed black contours and regions 1 to 5 are as in Figures 3a and 3b.

horizontal advection. In box 1, this process is essentially driven by current anomalies $\left(-u^{'}\cdot\bar{s}_x - v^{'}\cdot\bar{s}_y\right)$ (Figure 7a). These current anomalies correspond to a strengthening of the western boundary currents, in particular, the North Brazil Current (Figure 8, box 1). This current carries relatively fresh waters from the mouth of the Amazon River to box 1, and its freshening effect peaks in July.

In box 4, like in box 1, current anomalies $\left(-u^{'}\cdot\bar{s}_x - v^{'}\cdot\bar{s}_y\right)$ are also the main contributor of advection anomalies, which explains the negative SSS anomalies in this box. This is related to a strengthening of the Brazil current (Figure 8, box 4) that carries into this box less salty waters from the north until May. On the opposite, in the two boxes, and from May to August, there is a strong positive contribution (Figures 7a

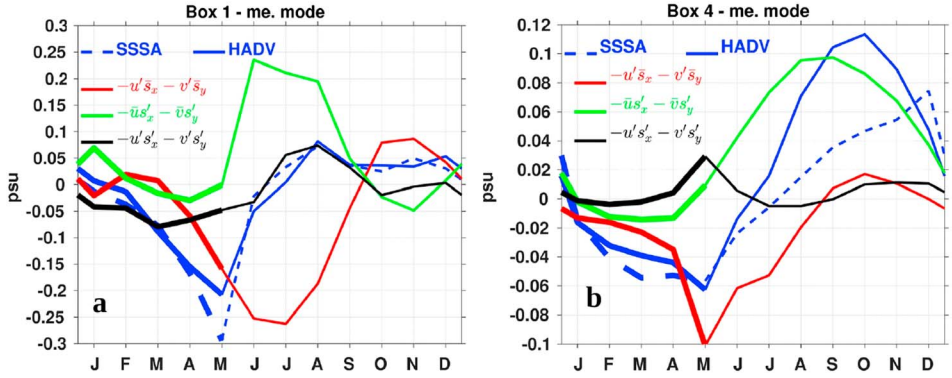


Figure 7. Time series of model SSS anomalies related to the meridional mode (blue dashed line), integrated horizontal advection anomalies (blue line) and their decomposition following equation (4) into term II (red line), term III (green line), and term IV (black line) in (a) box 1 (45–57°W, 6–16°N) and (b) box 4 (40–32°W, 11–20°S). All the time series are obtained by regressing the box-averaged interannual anomalies for each calendar month onto the spring meridional mode time series shown in Figure 2c. The January to May period corresponds to the development and the mature phase of the mode (heavy lines). SSS = sea surface salinity; SSSA = sea surface salinity anomaly; HADV = horizontal advection.

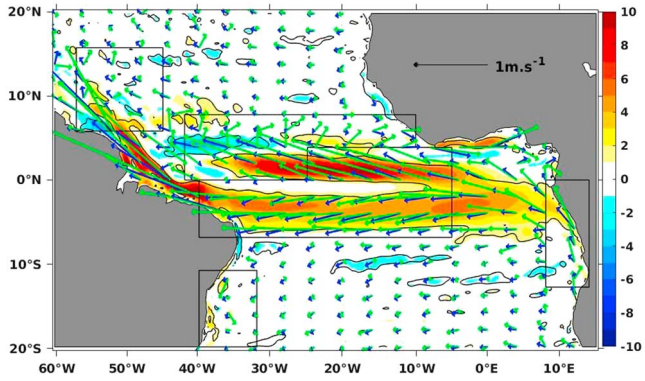


Figure 8. Surface current seasonal mean ($\overline{u}$, blue arrows), sum of the seasonal mean and interannual anomalies related to the meridional mode ($\overline{u} + 10u'$, green arrows), and amplitude of the interannual anomalies related to the meridional mode (cm/s, shading). Interannual anomalies related to the meridional mode correspond to regression coefficients of interannual anomalies onto the meridional mode time function shown in Figure 2c. The multiplicative coefficient 10 is chosen arbitrarily to highlight currents anomalies. This somewhat distorts the direction of these current vectors. The black contours represent the 90% significance threshold and boxes are as in Figure 3a.

and 7b) of the changes in SSS gradient on advection that partly compensate the contribution due to current anomalies. This advection process contributes to the decrease of SSS anomalies at the end of the spring meridional mode.

In box 5 off Congo River, positive SSS anomalies are due to horizontal advection south of the Congo outflow located at 6°S (Figure 6c) and subsurface processes north of this latitude (Figure 6d). This advection process, dominated by its meridional component (Figure 9a), is mostly related to a strengthening of the surface northward Angola current (Figure 8; Kopte et al., 2017) that carries fresh waters from the Congo River northward (Figures 9b and 8). Regarding the subsurface processes, vertical advection contributes more than diffusion (Figure 9a) because of the strong vertical salinity gradient created by the discharge of Congo River. This process brings saltier subsurface waters toward the surface.

3.4.2. Equatorial Mode

As done previously for the meridional mode, we also investigated the causes of the equatorial mode SSS signature. It generally shows that both oceanic and atmospheric forcing are important to explain the signature in each box (Figure 10).

In box 1, the SSS signature is clearly due to horizontal advection anomalies (Figure 10). They are controlled by SSS gradient anomalies ($-\overline{u}\cdot s_x' - \overline{v}\cdot s_y'$; Figure 11). The western boundary current likely advects anomalies created at the equator by an excessive precipitation (Figure 10b) toward this region.

In boxes 2 and 3, the SSS signature is due to both atmospheric forcing and horizontal advection. The atmospheric forcing dominates in box 3 because of a southward shift of the ITCZ that brings more rain into this box where SSS then decreases and less rain in box 2 where SSS increases (Figures 10a and 10b).

In box 2, in addition to this atmospheric forcing contribution, meridional advection is also important until September (Figures 12a and 12b). This is due to current anomalies combined with a strong mean meridional SSS gradient ($-v'\cdot\overline{s}_y$, Figure 12b), namely, current anomalies (Figure 13, box 2) that advect salty waters southward from the north subtropical gyre into box 2.

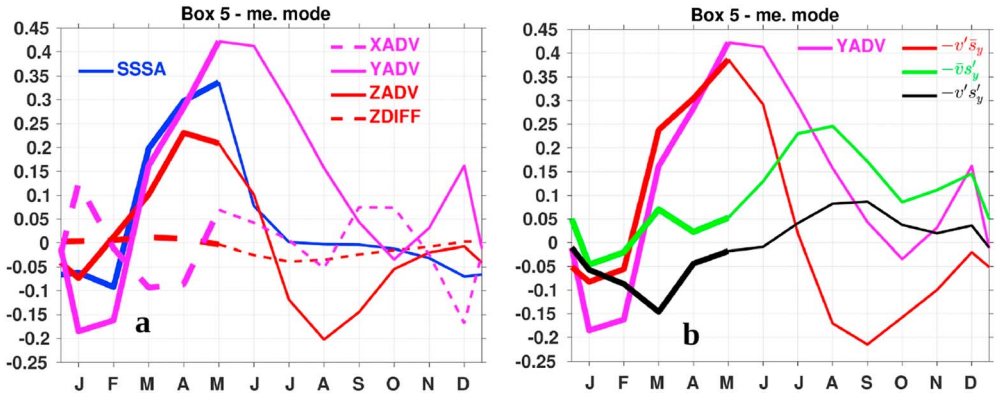


Figure 9. (a) Time series of SSS anomalies related to a positive meridional mode (blue line), zonal (magenta dashed line), meridional (magenta line) and vertical (red line) advection, and vertical diffusion (red dashed line); and (b) the different terms of the meridional advection (magenta line) decomposition following equation (4), into term II (red line), term III (green line), and term IV (black line) in box 5 (8–14°E, 13–0°S). All the time series are obtained by regressing the box-averaged interannual anomalies for each calendar month onto the spring meridional mode time series shown in Figure 2c. The period from January to May corresponds to the development and the mature phase of the mode (heavy lines). SSS = sea surface salinity; SSSA = sea surface salinity anomaly.

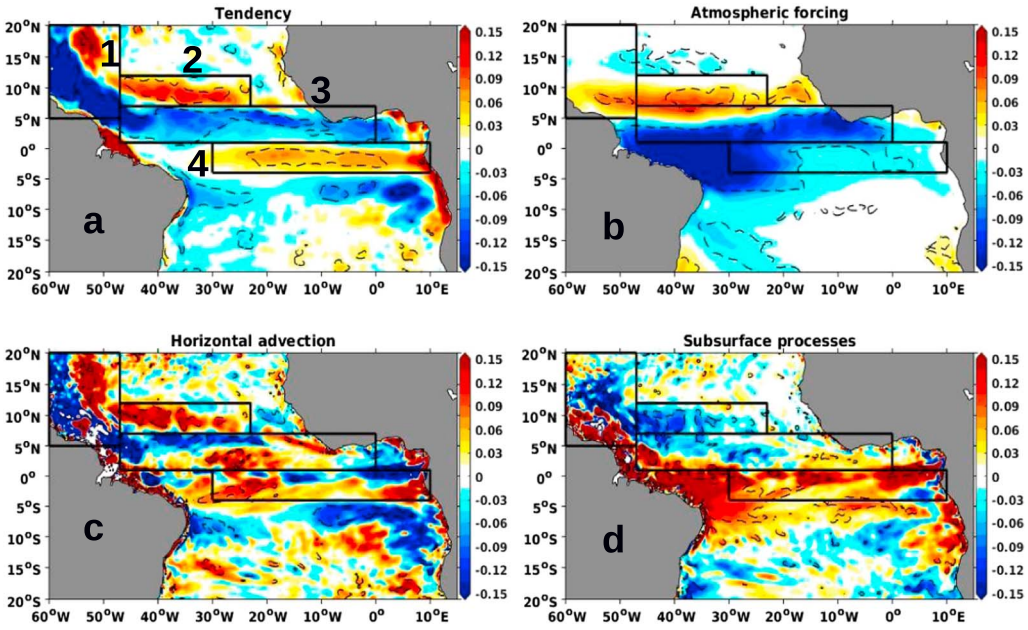


Figure 10. Spring to summer mixed-layer salinity budget (pss) for the equatorial mode: (a) tendency term, (b) atmospheric forcing, (c) horizontal advection, and (d) subsurface processes. Figures 10a–10d represent regression coefficients of salinity budget term anomalies onto the equatorial mode time function shown in Figure 2f. The dashed black contours and regions 1 to 4 are as in Figures 3d and 3e.

In box 4, positive SSS anomalies are mainly due to subsurface processes (Figure 10) and horizontal advection. The subsurface processes include vertical advection and diffusion. Figure 14 shows that the contributions of both terms are almost equal, while atmospheric forcing modulate them by its negative contribution. The contribution of the horizontal advection is due to the South Equatorial Current variation in this box (Figure 13).

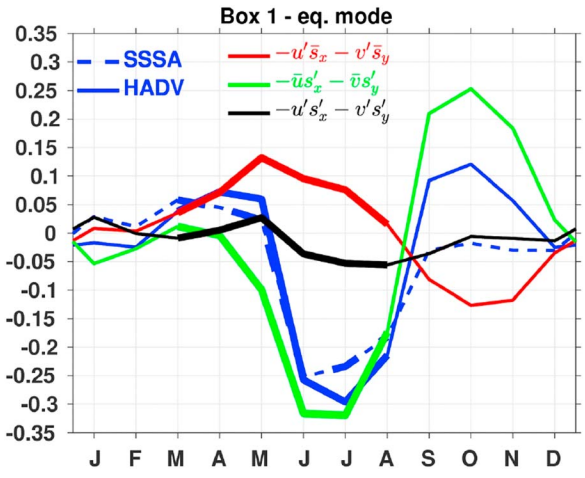


Figure 11. As Figure 7a but related to a positive equatorial mode in the western box 1 (60–47°W, 5–20°N), where only negative anomalies are averaged. All the time series are obtained by regressing the box-averaged interannual anomalies for each calendar month onto the summer equatorial mode time series shown in Figure 2f. The period from April to August corresponds to the development and the mature phase of the mode (heavy lines). SSSA = sea surface salinity anomaly; HADV = horizontal advection.

4. Summary and Discussion

The signature of the dominant tropical Atlantic interannual modes of climate variability, previously documented from SST and surface wind stress, was investigated on SSS using in situ and satellite-derived observations and a regional simulation. Both observations and model show that during the positive phase of the meridional mode, a north-south dipole of SSS anomalies appears along the equatorial region, with positive and negative anomalies around 5°S and 5°N, respectively. Negative SSS anomalies form off the South American coast around 15°S and 10°N. Positive SSS anomalies also form off the African coast with a maximum around 10°S. The equatorial mode has an SSS signature different from the meridional mode. During its positive phase, there are 2° to 5° wide zonal bands of SSS anomalies that are positive around 10°N, negative around 5°N, and then positive again around 3°S. There are strong negative SSS anomalies at 10°N off the South American coast. Due to the linear regression method we used to extract these SSS patterns, we can only assume that anomalies of opposite sign form during the negative phase of these two modes. This assumption is plausible for the equatorial mode as its SST and wind patterns are largely symmetric (Lübbecke & McPhaden, 2017). However, it is less likely for the meridional mode due to the equatorial asymmetric of the ITCZ and would require further investigation.

Moreover, since the positive equatorial and meridional mode events documented in terms of SST and surface wind stress anomalies in 2010 and

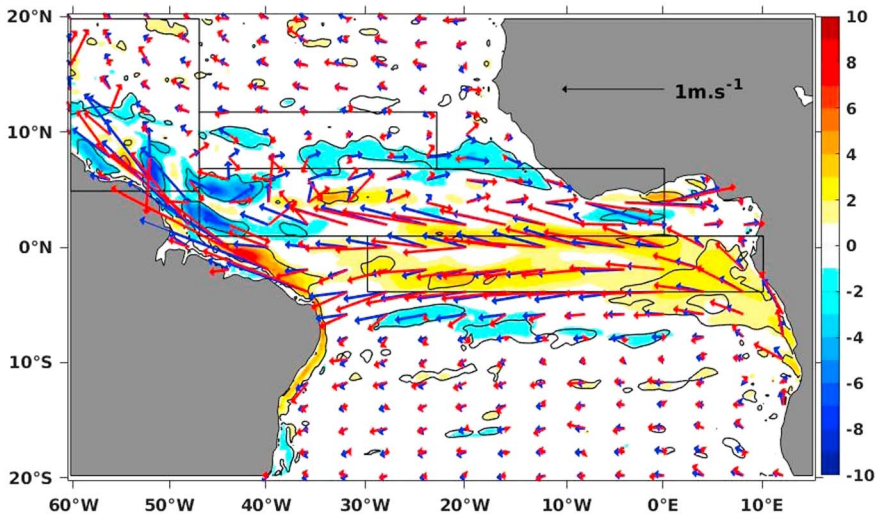


Figure 12. Surface current seasonal mean ($\overline{u}$, blue arrows), sum of the seasonal mean and interannual anomalies related to the equatorial mode ($\overline{u} + 10u'$, red arrows), and amplitude of the interannual anomalies related to the equatorial mode anomalies (cm/s, shading). Interannual anomalies related to the equatorial mode correspond to regression coefficients of interannual anomalies onto the equatorial mode time function shown in Figure 2f. The multiplicative coefficient 10 is chosen arbitrarily to highlight currents anomalies. This somewhat distorts the direction of these current vectors. The black contours represent the 90% significance threshold, and boxes are as in Figure 3a.

2012, respectively, are included in both the SMOS and in situ products' availability period, we compare the SSS anomalies observed in each product. A good agreement is observed between the previously extracted SSS signature and spring 2012 and summer 2010 in situ anomalies. In addition, there is a very good agreement between the in situ and SMOS-derived SSS modes, although the latter appears noisier due to its finer resolution. In areas where in situ data are not available, especially off Congo and Amazon rivers, SMOS fills the gap with anomalies very consistent with the expected SSS signature.

As the model reproduces consistently the observed SSS signature, we use it with confidence to diagnose the dominant physical mechanisms that are responsible for this signature. The diagnostic results show the following.

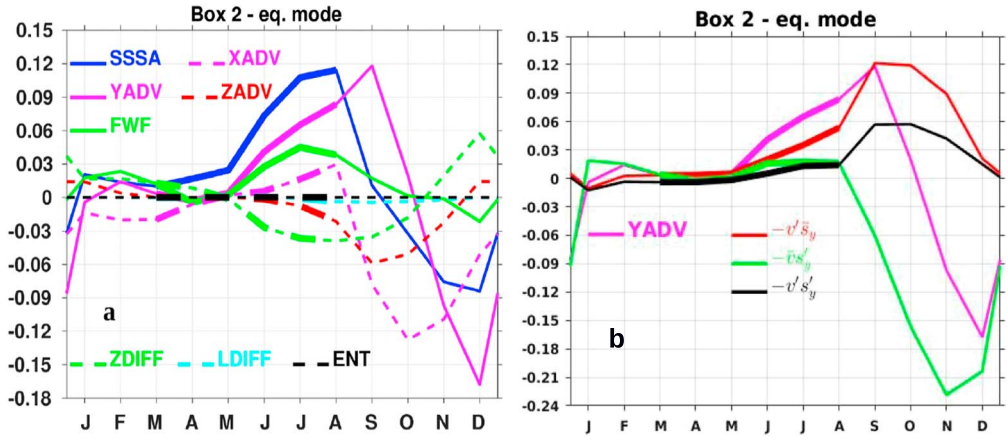


Figure 13. (a) Time series of SSS anomalies related to a positive equatorial mode (blue line); zonal (magenta dashed line), meridional (magenta line), and vertical (red dashed line) advection; freshwater flux (green line); vertical diffusion (green dashed line); lateral diffusion (light blue dashed line); and entrainment (black dashed line). And (b) the different terms of the meridional advection (magenta line) decomposition following equation (4), with term II (red line), term III (green line), and term IV (black line) in box 2 (47–23°W, 7–12°N). All the time series are obtained by regressing the box-averaged interannual anomalies for each calendar month onto the summer equatorial mode time series shown in Figure 2f. The period from April to August corresponds to the development and the mature phase of the mode (heavy lines). SSS = sea surface salinity; SSSA = sea surface salinity anomaly.

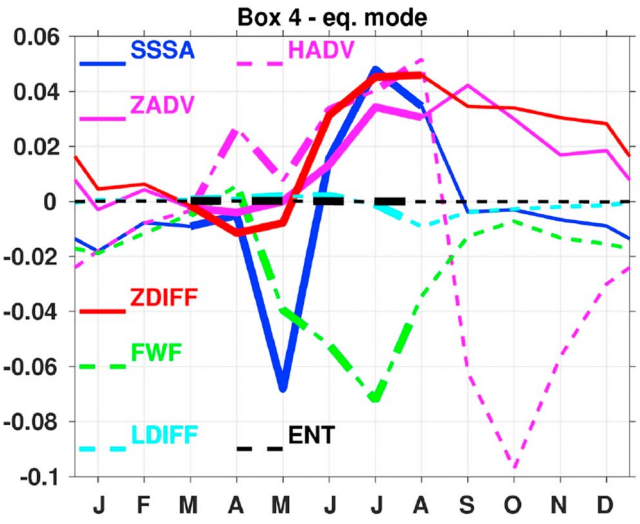


Figure 14. Time series of SSS anomalies (blue line), horizontal advection (magenta dashed line), vertical advection (magenta line), diffusion (red line), freshwater flux (green dashed line), lateral diffusion (light blue dashed line), and entrainment (black dashed line) in the south equatorial box (30°W–10°E, 4°S–1°N) during a positive equatorial mode. All the time series are obtained by regressing the box-averaged interannual anomalies for each calendar month onto the summer equatorial mode time series shown in Figure 2f. The period from April to August corresponds to the development and the mature phase of the mode (heavy lines). SSS = sea surface salinity; SSSA = sea surface salinity anomaly.

For the meridional mode, the north-south dipole observed in equatorial band is mainly due to the ITCZ northward shift associated with a positive meridional mode. As the ITCZ corresponds to a maximum in rainfall, this shift brings more rain in the northern part of the dipole yielding to a decrease of SSS and less rain in the southern part where SSS increases. Both strong negative SSS anomalies found off the South American coast are mainly due to changes in horizontal advection. To better understand these changes, we have deepened our investigation by decomposing the advection term into several components: the advection of mean or anomalous SSS gradient by anomalous or mean current. The results reveal that advection is essentially driven by western boundary current anomalies in these two regions. In the north, the North Brazil Current strengthens and carries Amazon plume waters northward and its freshening effect peaks in July. Meanwhile, in the south, the Brazil Current strengthens and carries relatively fresh waters southward along the coast with a peak in June. On the opposite, from May to December, after the meridional mode peak, advection due to SSS gradient anomalies overcomes the contribution due to current anomalies. The positive SSS anomalies off Congo River are due to meridional advection south of the Congo outflow located at 6°S and vertical advection north of this latitude. This meridional advection is related to a slowing down of the southward Angola current that carries fresh waters from the Congo River southward. Vertical advection brings saltier subsurface waters toward the surface because of the strong vertical salinity gradient created by the Congo discharge. These findings are mostly consistent with Da-Allada, du Penhoat, et al. (2014), although, in addition to these processes, they highlighted the importance of vertical diffusion to explain the interannual variability in this region. The latter process is very weak in our study, which may be due to our focus on the spring meridional mode only.

For the equatorial mode signature, we also found that both oceanic and atmospheric forcing are important to explain the zonal bands of positive and negative SSS anomalies around 10°N and 5°N, respectively. The southward shift of the ITCZ brings more rain into the region around 5°N where SSS decreases and less rain around 10°N where SSS increases. Also, the presence of a strong mean meridional SSS gradient favors the southward advection of salty waters from the north subtropical gyre into the region around 10°N. Precipitation changes related to the ITCZ shift, and meridional advection were also identified by Foltz and McPhaden (2008) as potential processes that can explain the SSS seasonal variations in these regions. Unlike in other regions, the SSS anomalies in south equatorial region are mainly driven by subsurface processes with contribution of both vertical advection and diffusion at the base of the mixed layer, while atmospheric forcing partly compensates them.

In both modes, horizontal advection clearly explains the strong negative SSS anomalies found at 10°N off the South American coast. This process was already identified as dominant in this region at both seasonal (Foltz & McPhaden, 2008) and interannual time scales (Ferry & Reverdin, 2004). However, the causes of the gradient anomalies that control the advection term during the equatorial mode is still unclear. It may be due to the precipitation-driven equatorial SSS anomalies, later advected by the North Brazil Current. Also, Tyaquiçã et al. (2017) suggest from a statistical analysis that SSS anomalies extending until 10°N can be produced by interannual variations in the Amazon flow, more clearly related to ENSO than Atlantic modes. Our model uses climatological runoff. This could lead to underestimation of SSS gradient anomalies and partly explain the driving role of current anomalies on advection that we found in the meridional mode. However, our model reproduces rather well the SSS anomalies in the Amazon plume in this configuration. It would be interesting to investigate further the influence of interannual Amazon flow changes on SSS. Comparing model simulations with and without interannual runoff would be instructive.

This study shows that both meridional and equatorial modes impact the SSS in tropical Atlantic through atmospheric and/or oceanic processes. The atmospheric forcing, related to ITCZ migration, controls the

equatorial region, while the advection, due to modulation of current dynamics, vertical gradient, and mixing at the base of the mixed layer, drives SSS in the region under the influence of river plumes.

Appendix A: Integration Method

Based on a methodology used to compute, from monthly fields, heat budget terms driving year-to-year SST variations (Alory & Meyers, 2009, Appendix B), we apply here a similar approach to compute, from daily fields, salt budget terms driving season-to-season SSS variations.

Consider S_i, the daily mean SSS for day i, and dS/dt_i, the different daily contribution terms of the salt budget equation (1).

Set $\Delta S_i = \frac{ds}{dt_i}\Delta t$

One can write the following:

$$\begin{aligned} S_{n+1} &= S_1 + \Delta S_1 + \Delta S_2 + \cdots + \Delta S_n \\ S_{n+2} &= S_2 + \Delta S_2 + \Delta S_3 + \cdots + \Delta S_n + \Delta S_{n+1} \\ S_{n+3} &= S_3 + \Delta S_3 + \Delta S_4 + \cdots + \Delta S_n + \Delta S_{n+1} + \Delta S_{n+2} \\ &\vdots \\ S_{n+n} &= S_n + \Delta S_n + \Delta S_{n+1} + \Delta S_{n+2} + \cdots + \Delta S_{n+n\text{-}1} \end{aligned} \tag{A1}$$

$$\begin{aligned} S_{n+1} + S_{n+2} + S_{n+3} + \ldots\ldots + S_{n+n} = S_1 + S_2 + S_3 + \cdots + S_n + \; & 1\times\Delta S_1 + 2\times\Delta S_2 + 3\times\Delta S_3 + \cdots \\ & + n\times\Delta S_n + (n-1)\times\Delta S_{n+1} + (n-2)\times\Delta S_{n+2} + \cdots + 1\times\Delta S_{n+n-1} \end{aligned} \tag{A2}$$

Adding up equation (A1), we obtain

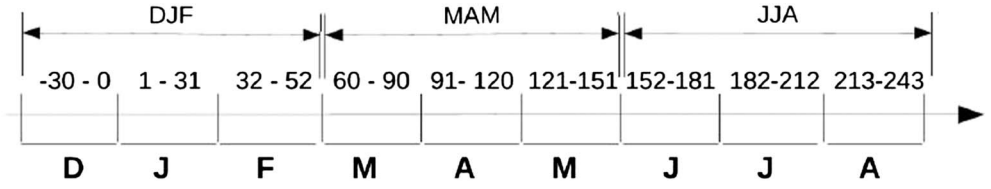
$$\sum_{i=n+1}^{n+n} S_i = \sum_{i=1}^{n} S_i + \sum_{i=1}^{n} i\times\Delta S_i + \sum_{i=1}^{n-1} (n-i)\times\Delta S_{n+i} \tag{A3}$$

which can be rewritten as

By dividing equation (A3) by n, we obtain the mean state

$$\frac{1}{n}\sum_{i=n+1}^{2n} S_i = \frac{1}{n}\sum_{i=1}^{n} S_i + \frac{1}{n}\left\{\sum_{i=1}^{n} i\times\Delta S_i + \sum_{i=1}^{n-1} (n-i)\times\Delta S_{n+i}\right\} \tag{A4}$$

with n = 92, the number of days in one season. Using calendar days (scheme below) and considering the development of SSS anomalies from winter to spring, when the meridional mode peaks, equation (A4) gives



$$S_i \rightarrow S_{-33+i} \text{ and } S_{n+i} \rightarrow S_{59+i}$$

$$\underbrace{\frac{1}{92}\sum_{i=93}^{184} S_{-33+i}}_{\overline{S_{60-151}}\;=\;\bar{S}_{MAM}} = \underbrace{\frac{1}{92}\sum_{i=1}^{92} S_{-33+i}}_{\overline{S_{-32-59}}\;=\;\bar{S}_{DJF}} + \frac{1}{92}\left[\sum_{i=1}^{92} i\times\Delta S_{-33+i} + \sum_{i=1}^{91} (92-i)\times\Delta S_{59+i}\right] \tag{A5}$$

Now considering the development of SSS anomalies from spring to summer, when the equatorial mode peaks, we have

$S_i \rightarrow S_{59+i}$ and $S_{n+i} \rightarrow S_{151+i}$

$$\underbrace{\frac{1}{92}\sum_{i=93}^{184} S_{59+i}}_{\overline{S_{152-243}}} = \underbrace{\frac{1}{92}\sum_{i=1}^{92} S_{59+i}}_{\overline{S_{60-151}}} + \frac{1}{92}\left[\sum_{i=1}^{92} i\times\Delta S_{59+i} + \sum_{i=1}^{91}(92-i)\times\Delta S_{151+i}\right] \tag{A6}$$

$\overline{S}_{JJA}$ $\overline{S}_{MAM}$

Here $\overline{S}_{DJF}$, $\overline{S}_{MAM}$, and $\overline{S}_{JJA}$ are the winter, spring, and summer mean SSS anomalies, respectively. The season-to-season contribution of SSS budget terms, including the different processes detailed in equation (1), is computed as a weighted mean of the daily model output.

Acknowledgments

The research leading to these results received funding from the EU FP7/2007-2013 under grant agreement 603521. It is part of M. F. A.'s PhD work funded by Institut de Recherche pour le Développement (IRD). It was also supported by the Centre National d'Etudes Spatiales (CNES) TOSCA-SMOS and OSTST-AltiETAO projects. The sea surface salinity gridded data (https://doi.org/10.6096%2FSSS-LEGOS-GRID-PAC) were produced and made freely available by the French Sea Surface Salinity Observation Service (http://www.legos.obs-mip.fr/observations/sss/). The reanalysis data were downloaded from ECMWF (http://www.ecmwf.int). The L3_DEBIAS_LOCEAN_v1 sea surface salinity maps have been produced by LOCEAN/IPSL (UMR CNRS/UPMC/IRD/MNHN) laboratory and ACRI-st company that participate to the Ocean Salinity Expertise Center (CECOS) of Centre Aval de Traitement des Donnees SMOS (CATDS). This product is distributed by the Ocean Salinity Expertise Center (CECOS) of the CNES-IFREMER Centre Aval de Traitement des Données SMOS (CATDS), at IFREMER, Plouzane (France).(https://www.catds.fr/Products/Available-products-from-CEC-OS/L3-Debiased-Locean-v1). Comments from anonymous reviewers helped to improve the manuscript.

References

Alory, G., & Delcroix, T. (2002). Interannual sea level changes and associated mass transports in the tropical Pacific from TOPEX/Poseidon data and linear model results (1964–1999). *Journal of Geophysical Research*, *107*(C10), 3153. https://doi.org/10.1029/2001JC001067

Alory, G., Delcroix, T., Téchiné, P., Diverrès, D., Varillon, D., Cravatte, S., et al. (2015). The French contribution to the voluntary observing ships network of sea surface salinity. *Deep-Sea Research*, *1*(105), 1–18. https://doi.org/10.1016/j.dsr.2015.08.00

Alory, G., & Meyers, G. (2009). Warming of the upper equatorial Indian Ocean and changes in the heat budget (1960–99). *Journal of Climate*, *107*(C10), 3153. https://doi.org/10.1029/2001JC001067

Berger, H., Tréguier, A., Perenne, N., & Talandier, C. (2014). Dynamical contribution to sea surface salinity variations in the eastern Gulf of Guinea based on numerical modeling. *Climate Dynamics*, *43*(11), 3105–3122. https://doi.org/10.1007/s00382-014-2195-4

Bosc, C., Delcroix, T., & Maes, C. (2009). Barrier layer variability in the western Pacific warm poolfrom 2000–2007. *Journal of Geophysical Research*, *114*, C06023. https://doi.org/10.1029/2008JC005187

Boutin, J., Martin, N., Kolodziejczyk, N., & Reverdin, G. (2016). Interannual anomalies of SMOS sea surface salinity. *Remote Sensing of Environment*, *180*, 128–136. https://doi.org/10.1016/j.rse.2016.02.053

Camara, I., Kolodziejczyk, N., Mignot, J., Lazar, A., & Gaye, A. T. (2015). On the seasonal variations of salinity of the tropical Atlantic mixed layer. *Journal of Geophysical Research: Oceans*, *120*, 4441–4462. https://doi.org/10.1002/2015JC010865

Carton, J. A., & Huang, B. (1994). Warm events in the tropical Atlantic. *Journal of Physical Oceanography*, *24*(5), 888–903. https://doi.org/10.1175/1520-0485(1994)024<0888:WEITTA>2.0.CO;2

Chang, P., Ji, L., Li, H., & Flügel, M. (1997). A decadal climate variation in the tropical Atlantic Ocean from thermodynamic air–sea interactions. *Nature*, *385*(6616), 516–518. https://doi.org/10.1038/385516a0

Curry, R., Dickson, B., & Yashayaev, I. (2003). A change in the freshwater balance of the Atlantic Ocean over the past four decades. *Nature*, *426*(6968), 826–829. https://doi.org/10.1038/nature02206

Da-Allada, Y. C., Alory, G., du Penhoat, Y., Jouanno, J., & Hounkonnou, N. M. (2014). Causes for the recent increase in sea surface salinity in the Gulf of Guinea. *African Journal of Marine Science*, *36*(2), 197–205. https://doi.org/10.2989/1814232X.2014.927398

Da-Allada, Y. C., Alory, G., du Penhoat, Y., Kestenare, E., Durand, F., & Hounkonnou, N. M. (2013). Seasonal mixed-layer salinity balance in the tropical Atlantic Ocean: Mean state and seasonal cycle. *Journal of Geophysical Research: Oceans*, *118*, 332–345. https://doi.org/10.1029/2012JC008357

Da-Allada, Y. C., du Penhoat, Y., Jouanno, J., Alory, G., & Hounkonnou, N. M. (2014). Modeled mixed-layer salinity balance in the Gulf of Guinea: Seasonal and interannual variability. *Ocean Dynamics*, *64*(12), 1783–1802. https://doi.org/10.1007/s10236-014-0775-9

Da-Allada, Y. C., Jouanno, J., Gaillard, F., Kolodziejczyk, N., Maes, C., Reul, N., et al. (2017). Importance of the Equatorial Undercurrent on the sea surface salinity in the eastern equatorial Atlantic in boreal spring. *Journal of Geophysical Research: Oceans*, *122*, 521–538. https://doi.org/10.1002/2016JC012342

Dai, A., & Trenberth, K. E. (2002). Estimates of freshwater discharge from continents: Latitudinal and seasonal variations. *Journal of Hydrometeorology*, *3*(6), 660–687. https://doi.org/10.1175/1525-7541(2002)003<0660:EOFDFC>2.0.CO;2

Dee, D. P., Uppala, S. M., Simmons, A. J., Berrisford, P., Poli, P., Kobayashi, S., et al. (2011). The ERA-Interim reanalysis: Configuration and performance of the data assimilation system. *Quarterly Journal of the Royal Meteorological Society*, *137*(656), 553–597. https://doi.org/10.1002/qj.828

Delcroix, T., & Hénin, C. (1991). Seasonal and interannual variations of sea surface salinity in the tropical Pacific Ocean. *Journal of Geophysical Research*, *96*, 22,135–22,150. https://doi.org/10.1029/91JC02124

Dessier, A., & Donguy, J. R. (1994). The sea surface salinity in the tropical Atlantic between 10°S and 30°N—Seasonal and interannual variations (1977–1989). *Deep-Sea Research*, *41*(1), 81–100.

Doi, T., Tozuka, T., & Yamagata, T. (2009). Interannual variability of the Guinea Dome and its possible link with the Atlantic Meridional Mode. *Climate Dynamics*, *33*(7-8), 985–998. https://doi.org/10.1007/s00382-009-0574-z

Durack, P. J., & Wijffels, S. E. (2010). Fifty-year trends in global ocean salinities and their relationship to broad-scale warming. *Journal of Climate*, *23*(16), 4342–4362. https://doi.org/10.1175/2010JCLI3377.1

Durack, P. J., Wijffels, S. E., & Matear, R. J. (2012). Ocean salinities reveal strong global water cycle intensification during 1950 to 2000. *Science*, *336*(6080), 455–458. https://doi.org/10.1126/science.1212222

Dussin, R., Barnier B., & Brodeau, L. (2016). The making of Drakkar forcing set DFS5. DRAKKAR/MyOcean Report 01-04-16, LGGE, Grenoble, France

Ferry, N., Parent, L., Garric, G., Bricaud, C., Testut, C.-E., Le Galloudec, O., et al. (2012). GLORYS2V1 global ocean reanalysis of the altimetric era (1992–2009) at mesoscale. *Mercator Quarterly Newsletter*, *44*, 29–39. Retrieved from http://www.mercator-ocean.fr/eng/actualites-agenda/newsletter

Ferry, N., & Reverdin, G. (2004). Sea surface salinity interannual variability in the western tropical Atlantic: An ocean general circulation model study. *Journal of Geophysical Research*, *109*, C05026. https://doi.org/10.1029/2003JC002122

Foltz, G. R., & McPhaden, M. J. (2008). Seasonal mixed layer salinity balance of the tropical North Atlantic Ocean. *Journal of Geophysical Research*, *113*, C02013. https://doi.org/10.1029/2007JC004178

Foltz, G. R., & McPhaden, M. J. (2010). Interaction between the Atlantic meridional and Niño modes. *Geophysical Research Letters*, *37*, L18604. https://doi.org/10.1029/2010GL044001

Friedman, A. R., Reverdin, G., Khodri, M., & Gastineau, G. (2017). A new record of Atlantic sea surface salinity from 1896 to 2013 reveals the signatures of climate variability and long-term trends. *Geophysical Research Letters*, *44*, 1866–1876. https://doi.org/10.1002/2017GL072582

Gasparin, F., & Roemmich, D. (2016). The strong freshwater anomaly during the onset of the 2015/2016 El Niño. *Geophysical Research Letters*, *43*, 6452–6460. https://doi.org/10.1002/2016GL069542

Gelderloos, R., Straneo, F., & Katsman, C. A. (2012). Mechanisms behind the temporary shutdown of deep convection in the Labrador Sea: Lessons from the Great Salinity Anomaly years 1968–71. *Journal of Climate*, *25*(19), 6743–6755. https://doi.org/10.1175/JCLI-D-11-00549.1

Gordon, A. L., Giulivi, C. F., Busecke, J., & Bingham, F. M. (2015). Differences among subtropical surface salinity patterns. *Oceanography*, *28*(1), 32–39. https://doi.org/10.5670/oceanog.2015.02

Grodsky, S. A., Reul, N., Lagerloef, G., Reverdin, G., Carton, J. A., Chapron, B., et al. (2012). Haline hurricane wake in the Amazon/Orinoco plume: AQUARIUS/SACD and SMOS observations. *Geophysical Research Letters*, *39*, L20603. https://doi.org/10.1029/2012GL053335

Hasson, A. E. A., Delcroix, T., Boutin, J., Dussin, R., & Ballabrera-Poy, J. (2014). Analyzing the 2010–2011 La Niña signature in the tropical Pacific sea surface salinity using in situ data, SMOS observations, and a numerical simulation. *Journal of Geophysical Research: Oceans*, *119*, 3855–3867. https://doi.org/10.1002/2013JC009388

Hasson, A. E. A., Delcroix, T., & Dussin, R. (2013). An assessment of the mixed layer salinity budget in the tropical Pacific Ocean, observations and modelling (1990–2009). *Ocean Dynamics*, *63*(2–3), 179–194. https://doi.org/10.1007/s10236-013-0596-2

Hastenrath, S., & Greischar, L. (1993). Circulation mechanisms related to north-east Brazil rainfall anomalies. *Journal of Geophysical Research*, *98*, 5093–5102. https://doi.org/10.1029/92JD02646

Hernandez, O., Jouanno, J., & Durand, F. (2016). Do the Amazon and Orinoco freshwater plumes really matter for hurricane-induced ocean surface cooling? *Journal of Geophysical Research: Oceans*, *121*, 2119–2141. https://doi.org/10.1002/2015JC011021

Hernandez, O., Jouanno, J., Echevin, V., & Aumont, O. (2017). Modification of sea surface temperature by chlorophyll concentration in the Atlantic upwelling systems. *Journal of Geophysical Research: Oceans*, *122*, 5367–5389. https://doi.org/10.1002/2016JC012330

Hormann, V., Lumpkin, R., & Foltz, G. R. (2012). Interannual North Equatorial Countercurrent variability and its relation to tropical Atlantic climate modes. *Journal of Geophysical Research*, *117*, C04035. https://doi.org/10.1029/2011JC007697

Hosoda, S., Suga, T., Shikama, N., & Mizuno, K. (2009). Global surface layer salinity change detected by *Argo* and its implication for hydrological cycle intensification. *Journal of Oceanography*, *65*(4), 579–586. https://doi.org/10.1007/s10872-009-0049-1

Hu, Z.-Z., & Huang, B. (2006). Physical processes associated with tropical Atlantic SST meridional gradient. *Journal of Climate*, *19*, 5500–5518.

Jouanno, J., Marin, F., du Penhoat, Y., Sheinbaum, J., & Molines, J.-M. (2011). Seasonal heat balance in the upper 100 m of the equatorial Atlantic Ocean. *Journal of Geophysical Research*, *116*, C09003. https://doi.org/10.1029/2010JC006912

Keenlyside, N. S., & Latif, M. (2007). Understanding equatorial Atlantic interannual variability. *Journal of Climate*, *20*(1), 131–142. https://doi.org/10.1175/JCLI3992.1

Kolodziejczyk, N., Boutin, J., Vergely, J.-L., Marchand, S., Martin, N., & Reverdin, G. (2016). Mitigation of systematic errors in SMOS sea surface salinity. *Remote Sensing of Environment*, *180*, 164–177. https://doi.org/10.1016/j.rse.2016.02.061

Kopte, R., Brandt, P., Dengler, M., Tchipalanga, P. C., Macuérie, M., & Ostrowski, M. (2017). The Angola Current: Flow and hydrographic characteristics as observed at 11°S. *Journal of Geophysical Research: Oceans*, *122*, 1177–1189. https://doi.org/10.1002/2016JC012374

Kushnir, Y., Robinson, W. A., Chang, P., & Robertson, A. W. (2006). The physical basis for predicting Atlantic sector seasonal-to-interannual climate variability. *Journal of Climate*, *19*(23), 5949–5970. https://doi.org/10.1175/JCLI3943.1

Large, W. G., & Yeager, S. G. (2004). Diurnal to decadal global forcing for ocean sea ice models: The data sets and flux climatologies. Rep. NCAR/TN-460+STR. Natl Cent for Atmos Res. Boulder, CO.

Levang, S. J., & Schmitt, R. W. (2015). Centennial changes of the global water cycle in CMIP5 models. *Journal of Climate*, *28*(16), 6489–6502. https://doi.org/10.1175/JCLI-D-15-0143.1

Lübbecke, J. F., Böning, C. W., Keenlyside, N. S., & Xie, S.-P. (2010). On the connection between Benguela and equatorial Atlantic Niños and the role of the South Atlantic Anticyclone. *Journal of Geophysical Research*, *115*, C09015. https://doi.org/10.1029/2009JC005964

Lübbecke, J. F., & McPhaden, M. J. (2017). Symmetry of the Atlantic Niño mode. *Geophysical Research Letters*, *44*, 965–973. https://doi.org/10.1002/2016GL071829

Madec, G., and the NEMO team (2016). NEMO ocean engine: Note du Pôle de modélisation de l''Institut Pierre-Simon Laplace No 27. Retrieved from http://www.nemo-ocean.eu/doc

Maes, C. (1998). Estimating the influence of salinity on sea level anomaly in the ocean. *Geophysical Research Letters*, *25*, 3551–3554. https://doi.org/10.1029/98GL02758

Maes, C., Ando, K., Delcroix, T., Kessler, W., McPhaden, M., & Roemmich, D. (2005). Observed correlation of surface salinity, temperature and barrier layer at the eastern edge of the western Pacific warm pool. *Geophysical Research Letters*, *33*, L06601. https://doi.org/10.1029/2005GL024772

Mama, A. C. & Alory, G. (2011). Influence des fleuves sur la salinité de l'Atlantique dans les modeles oceaniques (Master's thesis). CIPMA/UAC, Bénin. Retrieved from http://nodc-benin.org%2Fprojets%2Fpropao%2Factivit%26eacute%3Bs-propao-2.html

Mignot, J., & Frankignoul, C. (2004). Interannual to interdecadal variability of sea surface salinity in the Atlantic and its link to the atmosphere in a coupled model. *Journal of Geophysical Research*, *109*, C04005. https://doi.org/10.1029/2003JC002005

Murtugudde, R. G., Ballabrera-Poy, J., Beauchamp, J., & Busalacchi, A. J. (2001). Relationship between zonal and meridional modes in the tropical Atlantic. *Journal of Geophysical Research Letters*, *28*, 4463–4466. https://doi.org/10.1029/2001GL013407

Nobre, P., & Shukla, J. (1996). Variations of sea surface temperature, wind stress, and rainfall over the tropical Atlantic and South America. *Journal of Climate*, *9*, 2462–2479.

Reverdin, G., Kestenare, E., Frankignoul, C., & Delcroix, T. (2007). Surface salinity in the Atlantic Ocean (308S–508N). *Progress in Oceanography*, *73*(3-4), 311–340. https://doi.org/10.1016/j.pocean.2006.11.004

Richter, I., Behera, S. K., Masumoto, Y., Taguchi, B., Sasaki, H., & Yamagata, T. (2013). Multiple causes of interannual sea surface temperature variability in the equatorial Atlantic Ocean. *Nature Geoscience*, *6*(1), 43–47. https://doi.org/10.1038/ngeo1660

Schanze, J. J., Schmitt, R. W., & Yu, L. L. (2010). The global oceanic freshwater cycle: A state-of-the-art quantification. *Journal of Marine Research*, *68*(3), 569–595. https://doi.org/10.1357/002224010794657164

Schmitt, R. W. (1995). The ocean component of the global water cycle. *Reviews of Geophysics*, *33*, 1395–1409. https://doi.org/10.1029/95RG00184

Schmitt, R. W. (2008). Salinity and the global water cycle. *Oceanography*, *21*(1), 12–19. https://doi.org/10.5670/oceanog.2008.63

Servain, J., Wainer, I., McCreary, J., & Dessier, A. (1999). Relationship between the equatorial and meridional modes of climatic variability in the tropical Atlantic. *Journal of Geophysical Research Letters*, *26*, 485–488. https://doi.org/10.1029/1999GL900014

Singh, A., Delcroix, T., & Cravatte, S. (2011). Contrasting the flavors of El Niño-Southern Oscillation using sea surface salinity observations. *Journal of Geophysical Research*, *116*, C06016. https://doi.org/10.1029/2010JC006862

Tchilibou, M., Delcroix, T., Alory, G., Arnault, S., & Reverdin, G. (2015). Variations of the tropical Atlantic and Pacific SSS minimum zones and their relations to the ITCZ and SPCZ rain bands (1979–2009). *Journal of Geophysical Research: Oceans*, *120*, 5090–5100. https://doi.org/10.1002/2015JC010836

Terray, L., Corre, L., Cravatte, S., Delcroix, T., Reverdin, G., & Ribes, A. (2012). Near-surface salinity as Nature's rain gauge to detect human inflence on the tropical water cycle. *Journal of Climate*, *25*(3), 958–977. https://doi.org/10.1175/JCLI-D-10-05025.1

Tyaquiçã, P., Veleda, D., Lefèvre, N., Araujo, M., Noriega, C., Caniaux, G., et al. (2017). Amazon plume salinity response to ocean teleconnections. *Frontiers in Marine Science*, *4*, 250. https://doi.org/10.3389/fmars.2017.00250

Tzortzi, E., Josey, S. A., Srokosz, M., & Gommenginger, C. (2013). Tropical Atlantic salinity variability: New insights from SMOS. *Geophysical Research Letters*, *40*, 2143–2147. https://doi.org/10.1002/grl.50225

Tzortzi, E., Srokosz, M., Gommenginger, C., & Josey, S. A. (2016). Spatial and temporal scales of variability in tropical Atlantic sea surface salinity from the SMOS and Aquarius satellite missions. *Remote Sensing of Environment*, *180*, 418–430. https://doi.org/10.1016/j.rse.2016.02.008

Xie, S.-P., & Carton, J. A. (2004). Tropical Atlantic variability; patterns, mechanisms, and impacts. *Earth Climate Monograph*, *147*, 121–142.

Yu, L. (2011). A global relationship between the ocean water cycle and near-surface salinity. *Journal of Geophysical Research*, *116*, C10025. https://doi.org/10.1029/2010JC006937

Zhang, N., Feng, M., Du, Y., Lan, J., & Wijffels, S. E. (2016). Seasonal and interannual variations of mixed layer salinity in the southeast tropical Indian Ocean. *Journal of Geophysical Research: Oceans*, *121*, 4716–4731. https://doi.org/10.1002/2016JC011854